

Polar-Drive Implosions on OMEGA and the National Ignition Facility

Introduction

Polar drive (PD)¹ provides the capability to perform direct-drive-ignition experiments on laser facilities like the National Ignition Facility (NIF)² when cylindrically but not spherically configured for x-ray drive. Beams are absent near the equator in the x-ray drive configuration (Fig. 133.14). As a result, beams must be repointed to adequately irradiate the equator. This repointing of the beams results in oblique beams, which in turn result in laser energy deposition farther from the ablation surface, and consequently reduced kinetic energy of the imploding shell. Ignition designs^{3,4} compensate for this reduced hydrodynamic efficiency (defined as the ratio of the maximum shell kinetic energy to the laser energy) by increasing the energy of the most-oblique beams. To achieve adequate uniformity locally near the equator, these designs use beam profiles that include a skewed ellipse for the most-oblique beams. The combination of beam pointing, higher energies for the equatorial beams, and the skewed elliptical beam profiles results in nonradial (or lateral) gradients of the deposited laser energy and the temperature in the corona. Departures from the model predictions of deposited laser energy and lateral heat flow can play an important role in determining the symmetry of the

implosion. The goal of OMEGA and early NIF experiments is to develop and validate ignition-relevant models of laser deposition and heat conduction.

Several aspects of PD are similar to symmetrically driven direct-drive implosions. In the latter, beams are located around the target with spherical symmetry and irradiate the capsule more normally. In these schemes, the implosion velocity V_{imp} , defined as the maximum shell velocity, and the adiabat α_{inn} , defined as the ratio of the pressure to the Fermi-degenerate pressure averaged over the mass density that forms the high-density shell, are the most important parameters. The minimum energy for ignition E_{min} scales as⁵

$$E_{\text{min}} \text{ (kJ)} = 50.8 \alpha_{\text{min}}^{1.88} \left(\frac{V_{\text{imp}}}{3 \times 10^7 \text{ cm/s}} \right)^{-5.89} \left(\frac{P}{100 \text{ Mbar}} \right)^{-0.77},$$

where P is the ablation pressure. For both symmetric and polar drive, it is critical to achieve the designed implosion velocity while also setting the shell on the required adiabat. The implosion velocity and adiabat are primarily determined by one-dimensional (1-D) physics. The additional challenge in polar drive is multidimensional; it is necessary to adequately compensate for reduced energy coupling at the equator while achieving the required values of the adiabat and implosion velocity. Hydrodynamic simulations⁴ suggest that this compensation is achievable. The parameter space of adiabat and implosion velocity over which ignition is possible, including multidimensional effects, is therefore the same between the two direct-drive schemes.

Short-wavelength nonuniformities result from the imprinting of single-beam nonuniformities on the target. Subsequent multidimensional growth caused by the Rayleigh–Taylor (RT) instability⁶ influences the stability of the converging shell. Significant RT growth can degrade implosion performance. Since the number of e foldings of the most-dangerous mode to RT instability depends on the implosion velocity and details of the adiabat profile in the converging shell,⁷ which is very

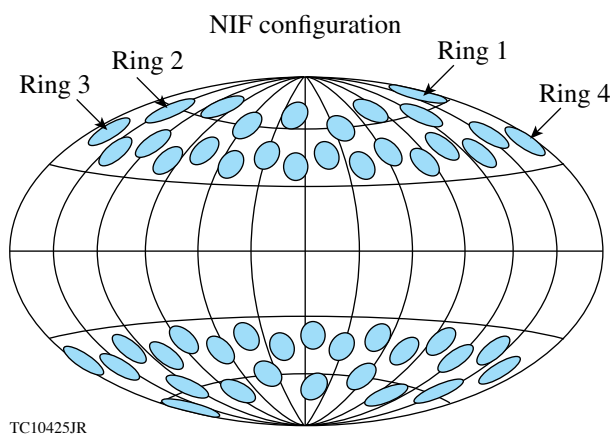


Figure 133.14
The NIF beam-port configuration arranged in four rings.

similar between PD and symmetric drive, short-wavelength behavior is very similar between the two schemes. Therefore, symmetric-drive implosions on OMEGA^{8–10} play an important role in validating models of laser imprint and RT growth that are also relevant for PD.

Polar drive differs from symmetric drive in the seeds that determine the low-mode asymmetry of the imploding shell and the hot spot. Beam geometry has a marginal influence on target symmetry and performance in symmetric drive. In PD, however, beam obliquity changes the angular and radial locations of the deposited laser energy. This influences the symmetry of the imploding shell. Seeds for long-wavelength nonuniformity are set throughout the laser pulse. Figure 133.15 shows the contours of laser energy deposited normalized to the volume as a function of radial location and polar angle for a NIF ignition design.⁴ Two aspects are unique to polar drive. The conduction zone (the distance between the ablation surface and the peak in deposited energy) is larger near the equator than at the pole, leading to lower hydrodynamic efficiency near the equator. There are significant transverse gradients in the deposited energy primarily because of the unique beam profiles and the higher power in the equatorial beams. These lateral gradients are insignificant in the symmetric design. Modeling this lateral heat flow is critical for an accurate prediction of symmetry in polar drive.

Shock nonuniformity is another important determinant of shell asymmetry. Long-wavelength shock-front perturbations, determined primarily by polar variations in the laser deposition [Fig. 133.16(a)], seed the nonuniformities on the inner shell surface [Fig. 133.16(b)]. The shocks shown in Fig. 133.16 are from an OMEGA-scale design with deliberate repointing

and mistiming to illustrate the seeding of perturbations at the rear shell surface. These perturbations grow when subsequent shocks reach the surface. Inner shell perturbations also grow as a result of the feedthrough of perturbations being seeded at the ablation surface determined by polar variations in laser-energy deposition and heat conduction. Accurate predictions of symmetry rely on accurate modeling of laser deposition and heat conduction.

Laser–plasma interactions (LPI’s) can compromise target performance by reducing implosion velocity, altering symmetry, and preheating the cold shell. Incorporating LPI effects within fluid codes is challenging because of the different length and time scales over which plasmas and fluids evolve. Empirical guidance is critical to understanding the magnitude of the effects of LPI processes and in improving designs to mitigate their deleterious effects. The goal of the early NIF experiments is to understand issues relating to energetics, symmetry, and preheat in NIF-scale plasmas.

In the following sections, OMEGA PD experiments are discussed with emphasis on adiabat and symmetry. The implosion velocity has been discussed in previous work.¹¹ Next, limitations of OMEGA experiments and early experiments planned for the NIF are discussed, followed by the conclusions.

OMEGA Experiments

The goal of OMEGA experiments is to predictably model target performance in polar drive. Twenty of the 60 OMEGA beams are omitted from the drive to emulate the 48-quad NIF x-ray-drive configuration [Fig. 133.17(a)].¹² The beams are then shifted toward the equator to directly drive the target more symmetrically. The 40 OMEGA beams can be considered to

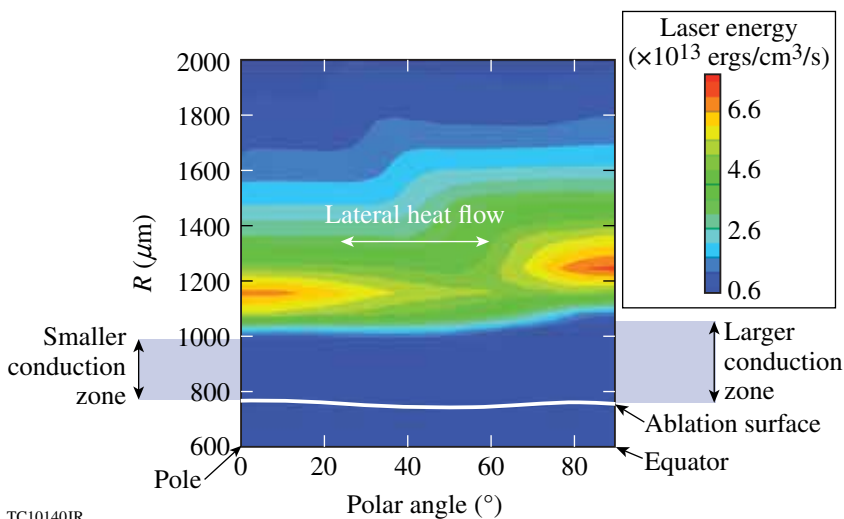


Figure 133.15

Density of laser energy deposited at the end of the laser pulse ($t = 9.0$ ns) for a NIF ignition design versus polar angle. The white line shows the location of the ablation surface. The conduction zone is larger at the equator, leading to reduced hydrodynamic efficiency. A significant transverse gradient in the deposited laser energy leads to transverse heat flow in polar drive.

TC10140JR

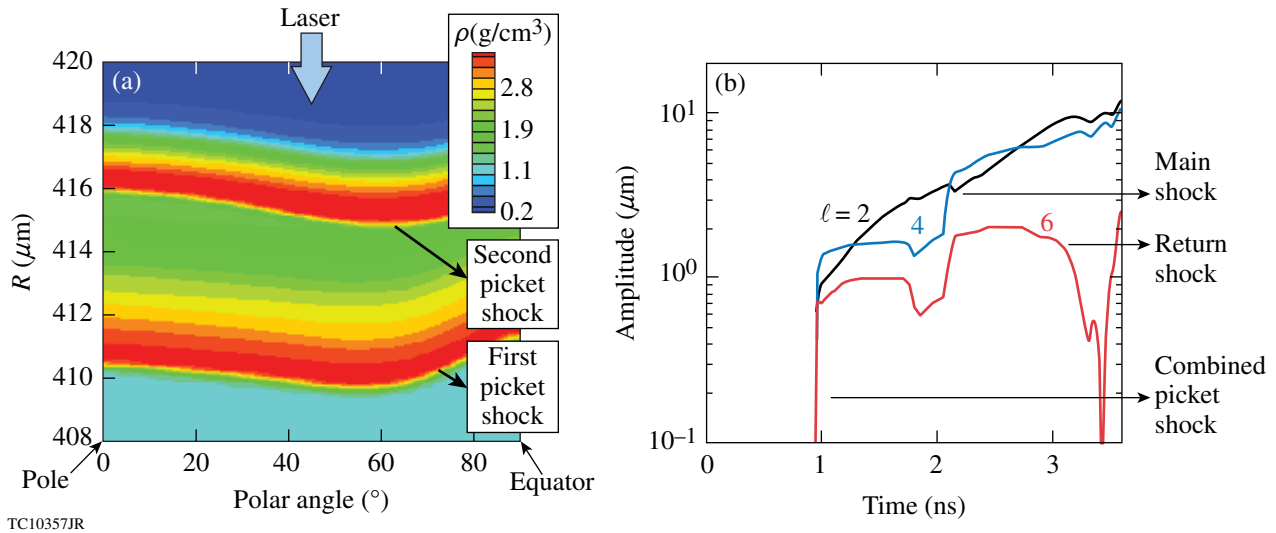


Figure 133.16

(a) Density contours at 650 ps showing nonuniform shocks from the first two pickets transiting the shell for an OMEGA PD design. (b) Perturbation amplitude at the rear shell surface is seeded by the shocks. Feedthrough from the ablation surface results in amplitude growth during acceleration and convergence (until 3 ns).

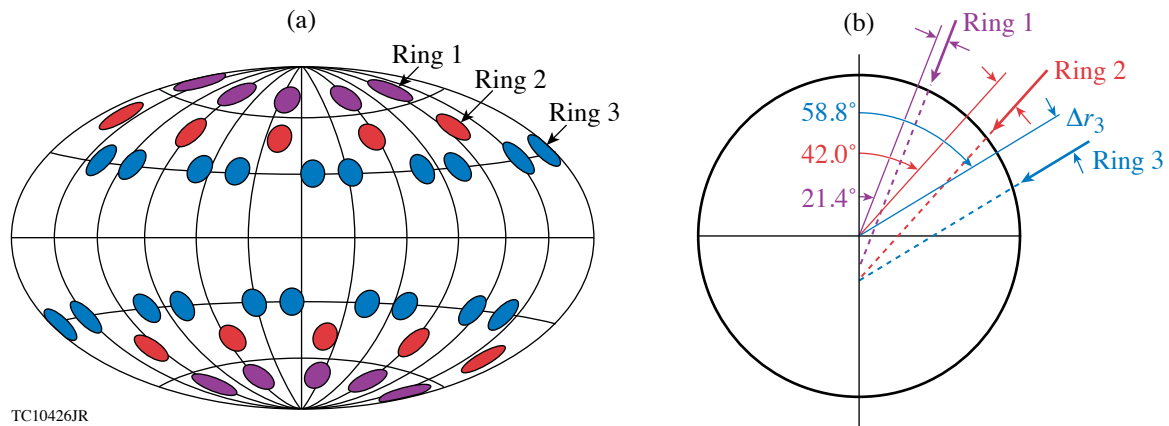


Figure 133.17

(a) The OMEGA beam port configuration with the equatorial beams omitted. There are three rings in each hemisphere. (b) Schematic showing the shifted beams for OMEGA PD geometry.

be arranged in three rings. Each ring is repointed only in polar angle by a distance Δr perpendicular to the beam axis (the azimuthal angles for OMEGA are already optimally pointed) [see Fig. 133.17(b)]. Each repointed configuration is characterized by three numbers $\{\Delta r_1, \Delta r_2, \Delta r_3\}$; larger values of these numbers correspond to more-oblique beams. Room-temperature experiments on OMEGA employ a 24- to 27- μm -thick plastic (CH) shell with 10 atm of deuterium (D_2) fill [see Fig. 133.18(a)]. Since 40 of the 60 beams are used, the energy on target is limited to approximately 13.5 kJ. (In principle, nearly 16 kJ can be obtained for PD implosions—these highest-energy implosions are reserved for cryogenic capsules.) A variety of laser pulse

shapes, with different temporal histories, irradiate the target. A flat foot to a continuous rise¹² [Fig. 133.18(b)] and three pickets preceding a main pulse are used^{11,13} [Fig. 133.18(c)]. The PD ignition design uses the latter pulse shape since nearly 1-D high areal densities have been demonstrated with this pulse shape in symmetric drive.¹⁴ In the room-temperature CH designs, both of these pulse shapes set the shell at a minimum adiabat of approximately 3.5. The continuous pulse shape irradiates the target at a higher peak intensity of $8 \times 10^{14} \text{ W/cm}^2$, while the triple-picket pulse irradiates the target at $4 \times 10^{14} \text{ W/cm}^2$ (these values are defined at the initial target radius). The advantage of the triple-picket pulse shape is the ability to achieve

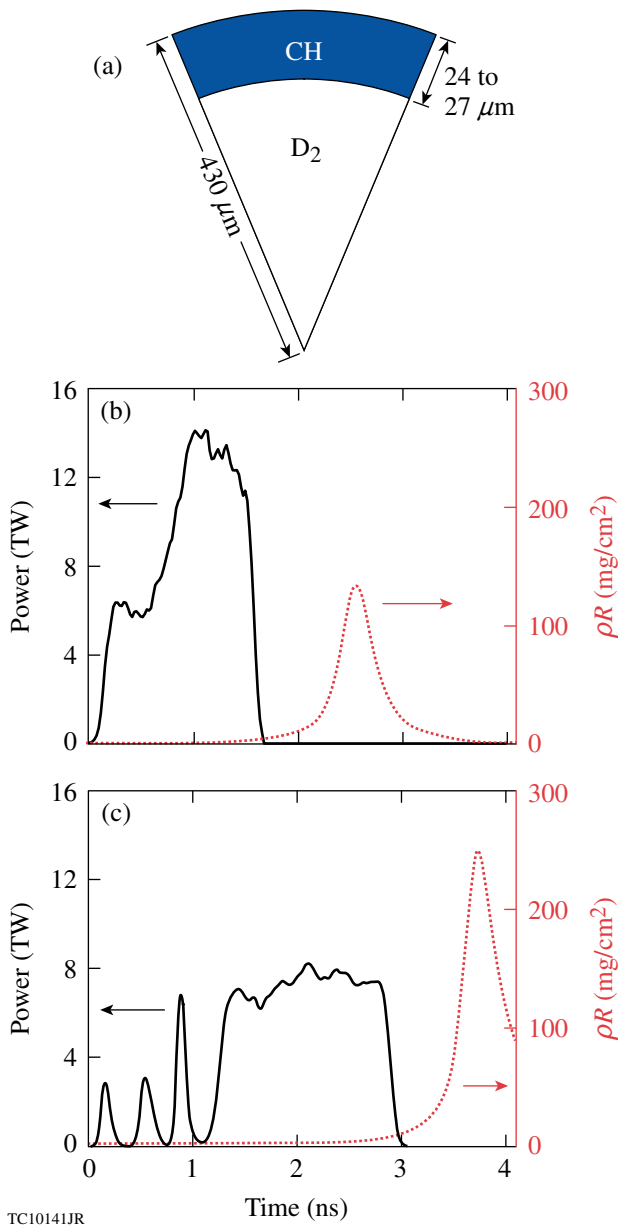


Figure 133.18
 (a) Schematic of the target used in PD implosion experiments on OMEGA. [(b) and (c)] Laser pulse (left axis) and simulated areal density averaged over the polar angle (right axis) for (b) the continuous pulse shape and (c) the triple-picket pulse shape.

higher convergence as explained below. Full beam smoothing (1/3-THz three-color-cycle smoothing by spectral dispersion¹⁵ and polarization smoothing¹⁶) is used. The implosion velocity of these capsules is approximately 2×10^7 cm/s. Higher velocities can be obtained in cryogenic implosions where the lower-density deuterium–tritium (DT) layer permits thicker shells and technically feasible spacing between the pickets for less-massive targets.¹¹ Target performance is studied from

measurements of areal density (ρR) and x-ray images obtained by backlighting the converging shell using a subset of the beams omitted from the drive. Other measures of target performance such as yield, neutron rate history, and the related implosion velocity have been presented elsewhere.¹¹

The predicted areal densities for the two pulse shapes discussed in this work differ quite significantly. The triple-picket pulse maintains the drive pressure until the shock is reflected from the center of the converging capsule, whereas the continuous pulse permits the shell to coast and decompress, reducing the areal density. Figure 133.19 shows the mass density and adiabat profile for the two pulse shapes at the end of the laser

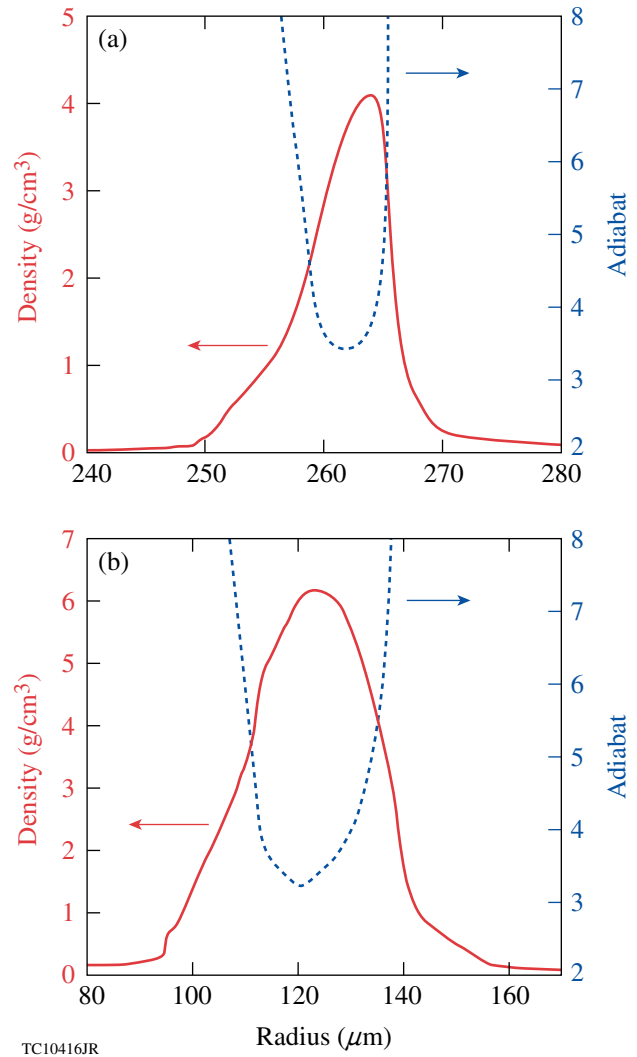


Figure 133.19
 Mass-density profile at the end of the laser pulse (left axis) and adiabat profile in the converging shell (right axis) for (a) the continuous pulse shape and (b) the triple-picket pulse shape.

pulse; while the adiabat profiles are very similar, the shell has traveled a greater distance for the triple-picket pulse shape. At peak neutron production, the shell in the implosion driven with the triple-picket pulse is simulated to have higher convergence (the convergence ratio is $CR \sim 19$ compared to $CR \sim 13$ for the continuous laser pulse) and to have a higher density than the shell driven with the continuous pulse shape.

The areal density is inferred in implosion experiments through the energy loss of secondary protons¹⁷ and is inferred only during neutron production. To compare the areal density from simulations with that inferred from observations, it is important to account for the observed neutron production history.⁸ Figure 133.20(a) shows the measured and simulated rates

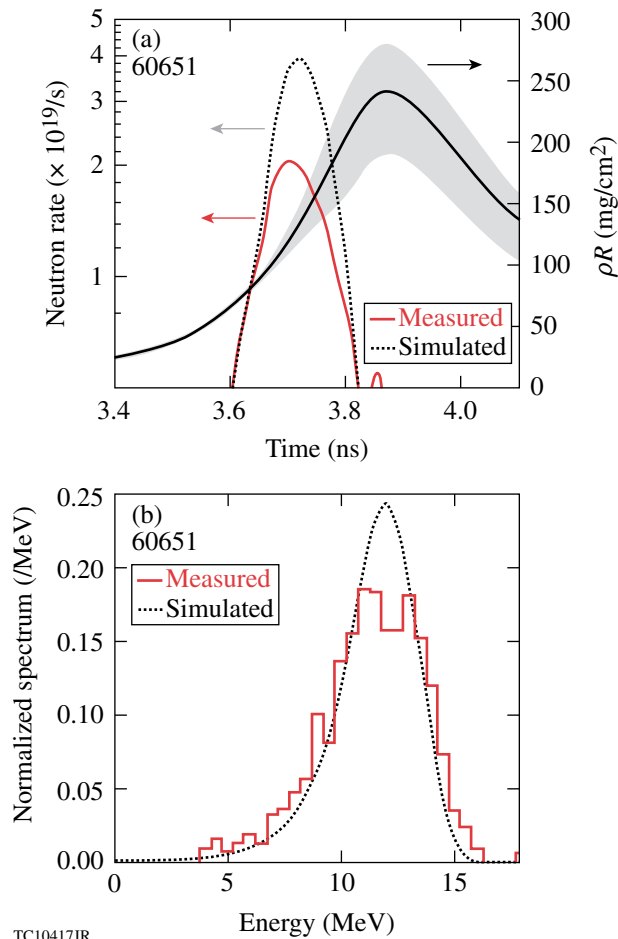


Figure 133.20
 (a) Simulated neutron rate (dotted line, left axis) overlaid on the measured neutron rate (red line, left axis), and the polar-angle averaged areal-density history (solid line, right axis). The shaded region indicates the minimum and maximum areal density in polar angle. (b) Measured (solid) and simulated (dotted) secondary proton spectrum.

for neutron history overlaid with the areal-density evolution for a PD implosion driven with a triple-picket pulse shape and beam repointing corresponding to $\{90 \mu m, 150 \mu m, 150 \mu m\}$. The simulations were performed with the hydrodynamic code *DRACO*¹⁸ including a full 3-D laser ray trace,¹⁹ collisional absorption as the only laser-energy deposition mechanism, a flux-limited heat-conduction model (with a flux limiter $f = 0.06$) (Refs. 20 and 21), and multigroup diffusive radiation transport with astrophysical opacity tables. The experimental neutron rate history is measured using the neutron temporal diagnostic.²² The *DRACO*-simulated profiles are post-processed with the particle-tracking code *IRIS*²³ using this measured rate history to calculate the emergent proton spectrum. Excellent agreement is obtained in the spectrum, as seen in Fig. 133.20(b), indicating that the adiabat is modeled well for this pulse shape. The areal density from the continuous pulse shape has been published previously.¹¹ The trend across pulse shapes is recovered experimentally as seen in Fig. 133.21. For an implosion with no coasting phase, the maximum areal density has been shown to depend primarily on the adiabat²⁴ as $\rho R_{max} (mg/cm^2) = [2.6 \times 10^2 E_L^{1/3} (kJ)] / \alpha_{inn}^{0.6}$, where E_L is the laser energy. Simulations reproduce the areal density for both pulse shapes, indicating that *DRACO* accurately models shock timing and the effect of coasting on compression. This result is consistent with independent PD shock-timing measurements using cone-in-shell geometries.¹³

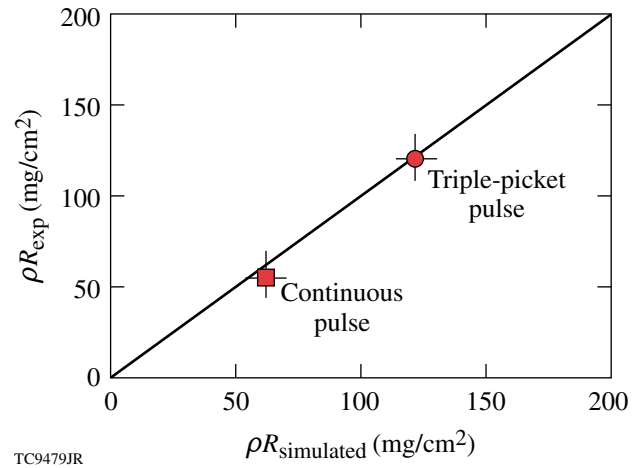


Figure 133.21
 Inferred areal density compared to simulated values for the continuous and triple-picket pulse shapes. The vertical error bars represent the standard deviation of the four areal-density measurements around the target chamber center for each shot. The horizontal error bars represent the standard deviation of the inferred areal density in polar angle from the simulated spectra.

Backlit images indicate that simulations reproduce the gross features of the converging shell. Figure 133.22 shows the images obtained by backlighting the converging shell with an ~ 4.7 -keV Ti backlighter for two different pointing configurations, corresponding to $\{90 \mu\text{m}, 150 \mu\text{m}, 150 \mu\text{m}\}$ and $\{30 \mu\text{m}, 150 \mu\text{m}, 150 \mu\text{m}\}$, for the triple-picket pulse shape. *DRACO* simulations are post-processed with the code *Spect3D*,²⁵ which transports x rays through the *DRACO* profiles accounting for absorption using opacities generated by the PRISM group.²⁵ The plasma is assumed to be in local thermodynamic equilibrium (LTE), which is an excellent assumption for the densities (from solid up to $\sim 150 \text{ g/cm}^3$) and temperatures (from $\sim \text{eV}$ up to $\sim \text{keV}$) characteristic in the compressing capsule. The detector resolution and the time window over which the images are integrated in the experiment are included in the postprocessing. The simulations reproduce the measured images very well. The images shown in Fig. 133.22 correspond to the latest time at

which the shell can be unambiguously viewed. At this time the shell has converged by approximately a factor of 5. Later in time the backlighter intensity is significantly lower than the self-emission from the compressed core, precluding an inference of the symmetry. For the first pointing configuration, the converging shell is prolate, for which one can correct by repointing Ring 1 closer to the pole. The second pointing configuration achieves a rounder core as seen in the images. The contour of maximum x-ray absorption (white line in Fig. 133.22) is decomposed into Legendre modes ℓ . The normalized mode amplitudes (defined as the ratio of the mode amplitude to the radius of maximum absorption) for $\ell = 2$ to 10 are in reasonable agreement between simulation and measurement. The typical error in the amplitude measurement is estimated to be of the order of 2% to 3%. The best observed uniformity with only repointing to correct for PD geometry has been obtained with the $\{30 \mu\text{m}, 150 \mu\text{m}, 150 \mu\text{m}\}$ configuration.

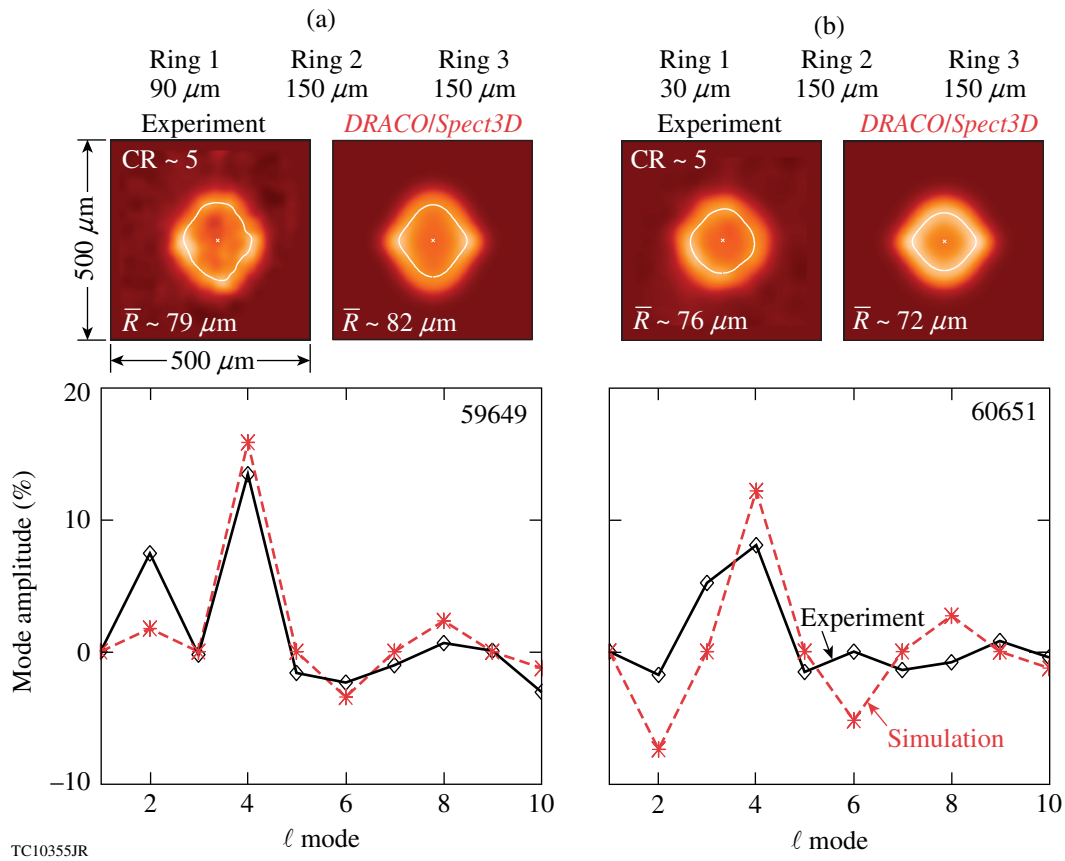


Figure 133.22

(a) Backlit image from the experiment together with the simulated image for the triple-picket pulse shape. The white lines indicate the contour of maximum absorption. The graphs show experimental and simulated normalized Legendre-mode amplitudes (the ratio of mode amplitude to average radius \bar{R}) of the contour of maximum absorption. (b) Same as (a) but for a different pointing that reduces the amplitude of the $\ell = 2$ Legendre mode.

Experimental and simulated backlit images for the two different pulse shapes for the same pointing configuration $\{90 \mu\text{m}, 120 \mu\text{m}, 120 \mu\text{m}\}$ are compared for the continuous pulse shape [Fig. 133.23(a)] and the triple-picket pulse shape [Fig. 133.23(b)]. With this pointing configuration there is an observable difference in the shape of the core for the two pulse shapes, which is reproduced by simulation. Excellent agreement is obtained in the modal amplitudes of the shell perturbations.

Current high-convergence OMEGA PD implosions can only be driven at low intensities owing to the limited energy available from 40 beams combined with the fixed spot size produced by OMEGA's existing phase plates (860 μm diameter corresponding to 95% of the energy enclosed).²⁶ Higher on-target intensities can be obtained with smaller targets and phase plates with smaller focal spots.¹¹ New phase plates have been obtained for the OMEGA laser, and experiments to study PD implosions at ignition-relevant intensities will begin in the near future.

NIF ignition targets have a radius that is nearly $4\times$ the radius of OMEGA-scale targets. Consequently, the density scale lengths in the corona of NIF targets are larger by the same ratio. As discussed in the next section, laser-plasma interactions become increasingly important to target performance for larger scale lengths. Experiments at the NIF scale are critical to understanding the role of these interactions on target performance.

Early NIF Experiments

The radial coronal density scale length in typical NIF ignition designs⁴ is $\sim 600 \mu\text{m}$, compared to the OMEGA-scale density scale length of $\sim 150 \mu\text{m}$. The magnitude of LPI effects typically increases with scale length. LPI can influence shell adiabat,²⁷ energetics,²⁸ and symmetry.²⁹ Two-plasmon decay (TPD)³⁰ primarily determines the extent of fast-electron pre-heat in implosions. Energetic electrons, accelerated by plasma waves, deposit their energy in the cold shell, raising its adiabat,

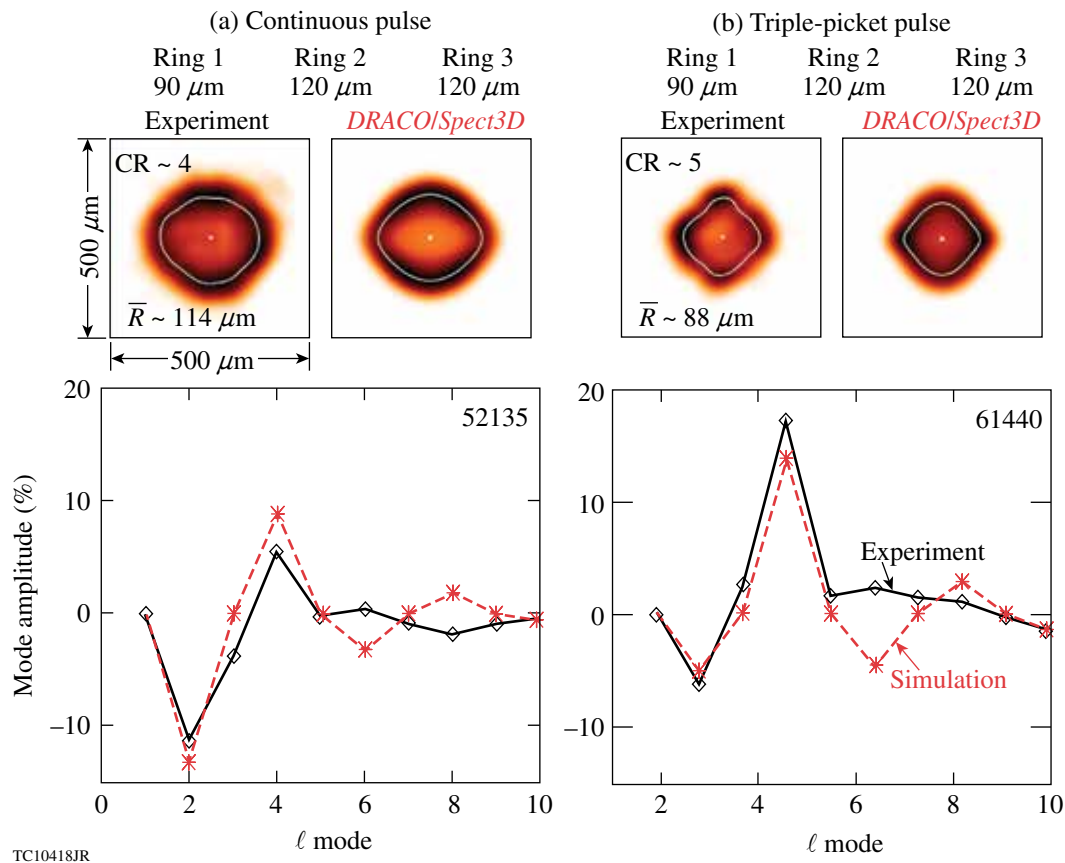


Figure 133.23

Experimental and simulated backlit images for the same pointing $\{90 \mu\text{m}, 120 \mu\text{m}, 120 \mu\text{m}\}$ but for the two different pulse shapes: (a) the high-intensity continuous pulse shape and (b) low-intensity triple-picket pulse shape. The white line indicates the contour of maximum absorption. The graphs show normalized Legendre-mode amplitudes (the ratio of mode amplitude to average radius \bar{R}) of the contour of maximum absorption.

making it more difficult to achieve the required compression. The extent of preheat is typically diagnosed by measuring energetic (“hard”) x rays (≥ 50 keV) produced by fast electrons.³¹ The threshold parameter for the TPD instability, defined as $\eta = I_{n/4} (10^{14} \text{ W/cm}^2) L_{n/4} (\mu\text{m}) / 233 T_{n/4}^e (\text{keV})$ (Ref. 30), where $I_{n/4}$, $L_{n/4}$, and $T_{n/4}^e$ are the laser intensity, density scale length, and the electron temperature at the quarter-critical surface, respectively, has been shown to correlate with the observed hard x-ray signal in OMEGA symmetric-drive implosions.³² However, the effect of this preheat on target performance in ignition-relevant OMEGA implosions is negligible.³³ The longer NIF scale lengths are suggestive of a higher threshold parameter and greater preheat from fast electrons; however, no clear physical mechanism links the threshold parameter to the observed hard x-ray signal. The threshold parameter has been defined in planar geometry for the absolute instability. TPD has also been shown to be convectively unstable³⁴ for the plasma conditions and profiles in direct-drive implosions, and this aspect is not included in the threshold parameter. Additionally, calculations of TPD indicate that this instability can become highly nonlinear and saturate.³⁵ Without detailed modeling of TPD, observations of hard x rays on the NIF are necessary to determine the extent of preheat.

In cross-beam energy transfer (CBET), incoming rays transfer their energy to outgoing rays through ion-acoustic waves.²⁸ This results in reduced laser-energy deposition and reduced hydrodynamic efficiency. The gain rate for CBET is $L^{-1} \sim (I_1 I_2) / [\nu_a^2 \eta^2 + (1 - \eta^2)^2]$ (Ref. 28), where I_1 and I_2 are the intensities of the two beamlets, ν_a is the damping rate of the ion-acoustic waves, and $\eta = \mathbf{k}_a \cdot \mathbf{u} - \omega_a / k_a c_a$ (the resonance condition where \mathbf{k}_a is the ion-acoustic wave vector, \mathbf{u} the fluid velocity, ω_a the ion-acoustic wave frequency, and c_a the ion-acoustic wave speed). Irradiating capsules with the relevant intensities (I_1 and I_2) is critical to understanding CBET effects. CBET reduces implosion velocity by $\sim 10\%$ in symmetric-drive OMEGA-scale implosions.²⁸ PD implosions indicate a reduced implosion velocity although the exact mechanism is not yet understood.¹¹ As presented earlier, however, symmetry in PD implosions is reproduced well with simulations that do not include CBET. This may be caused by either the negligible effect of CBET on symmetry in OMEGA-scale implosions or the relatively early time when the converging shell is viewed. When velocity scale lengths are long, as in the NIF-scale coronal plasma, the resonance condition for CBET is satisfied over a larger volume. This likely results in a greater level of CBET. NIF experiments are again important in identifying the extent of CBET.

Room-temperature CH implosions are planned for initial NIF experiments [Fig. 133.24(a)]. The first set of experiments are planned at lower intensities where LPI effects such as TPD and CBET are less important, enabling one to validate models in *DRACO* that do not contain these LPI effects. Future experiments will probe higher-intensity implosions to develop and validate models in that regime and identify mitigating strategies if required. To obtain the scale of the initial set of implosions, consider the scaling law $E \sim R_t^3$, which retains the same laser energy density per target volume, where E is the laser energy and R_t is the target radius. Using OMEGA energies of 25 kJ

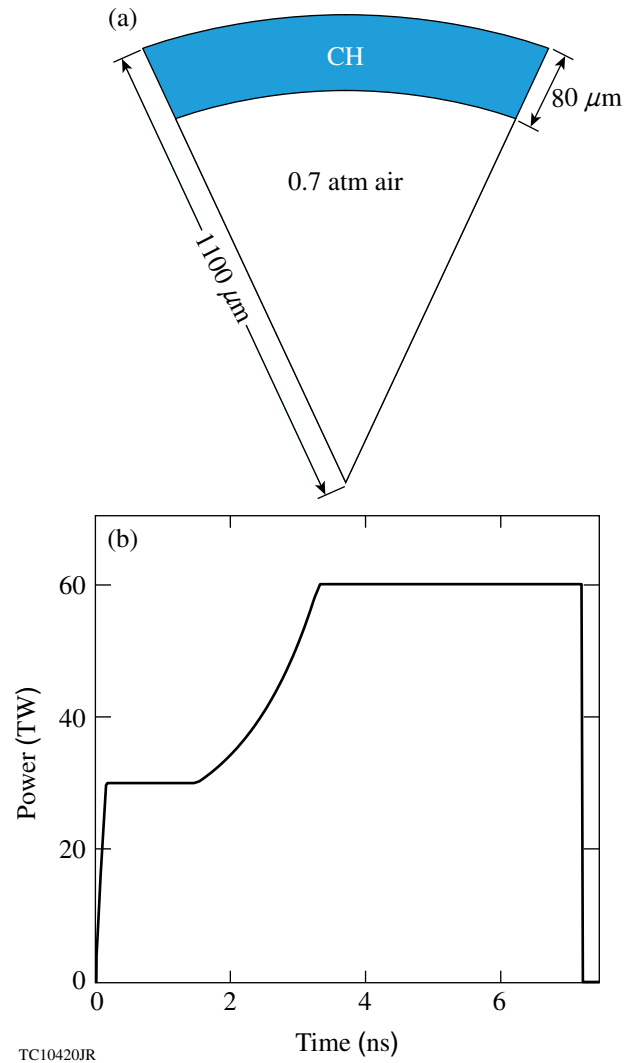


Figure 133.24

(a) Schematic of the target for early NIF experiments; (b) pulse shape from the 1-D design.

and the desired target radius of $\sim 1100 \mu\text{m}$ (this is determined by the NIF phase plates³⁶), these implosions must be driven with $\sim 350 \text{ kJ}$. Using $P \sim R_t^2$ yields a peak power of $P \sim 50 \text{ TW}$ and $T \sim R_t$ yields a pulse length of $T \sim 7.5 \text{ ns}$. The laser pulse shape [Fig. 133.24(b)]—a low foot to a continuous rise, similar to the OMEGA pulse shape described earlier—sets the target at a low adiabat of ~ 3 . These early experiments will use the existing NIF hardware including phase plates and single-beam smoothing. Beams are defocused³⁷ to achieve the optimal symmetry in the simulation. Beam phase fronts for the near field³⁶ are forward propagated using Fourier transforms to obtain the on-target beam shapes using the code *Waasikwa*.³⁸ The laser-related parameters of the design are shown in Table 133.V. In this reprinted configuration, some quads (a set of four beams form a quad) from the 44.5° cone are moved to 46° , while others are moved to 69° . Beams are repointed in azimuth to locations defined in Ref. 4. While this achieves excellent uniformity in the polar angle, it introduces an $\sim 10\%$ peak-to-valley, $\ell = 4$ variation in azimuth of the absorption because of the limited (four in each hemisphere) quads illuminating near a polar angle of 69° . This azimuthal variation can be reduced to 4% or lower with an $\ell = 8$ variation instead by splitting the 44.5° quads with two of the beams pointed to 46° and the remaining two to 69° . This splitting of the quads is not used in this work but is being investigated for future designs.

The on-target intensity from each of the rings is shown in Fig. 133.25. Rings 1 and 2 primarily irradiate the target near the pole, whereas the re-shifted Rings 3a, 3b, and 4 irradiate more toward the equator. The overlapped on-target intensity is higher near the equator. This is necessary to compensate for the reduced hydrodynamic efficiency from the more-oblique beams. Shock breakout is nearly uniform with this configuration of beam pointing, laser defocus, and pulse shapes except near the equator (Fig. 133.26). This significantly reduces core temperatures by injecting a jet of shell material into the hot spot

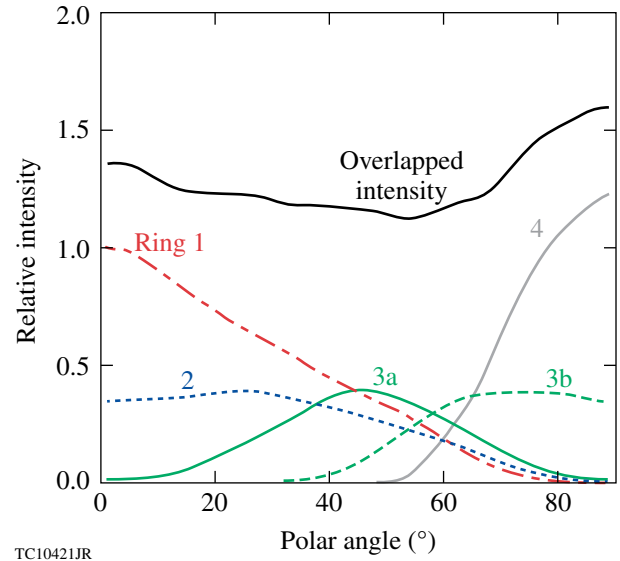


Figure 133.25

Intensity on target for the different rings at time $t = 0$. Rings 1 and 2 have peak irradiances near the pole. The shifting of Rings 3a, 3b, and 4 results in higher intensities toward the equator. The overlapped intensity is shown in black. Beams have been defocused and repointed (Table 133.V) to achieve this irradiation profile.

and radiatively cooling it. This can be corrected by designing an appropriate beam profile, as has been done for the ignition design, with the secondary ellipse on the equatorial beams.

For given pointing and defocus parameters, shell symmetry can be changed from spherical to prolate and oblate by changing the temporal pulse shapes, while maintaining the overall energy on target at $\sim 350 \text{ kJ}$ (see Fig. 133.27). The foot portion of the pulse, which determines the shock strength, is held constant among the three cases. Therefore, adjustments to the shape of the imploded shell can be made by varying the peak-power portions of the pulse shapes.

Table 133.V: The repointing and beam defocus used for the NIF design presented in the text. The pointing shift is as defined in Fig. 133.17: $\Delta r = R_t \times \sin(\theta_r - \theta)$, where R_t is the target radius.

Rings	Original port angle ($^\circ$) θ	Repointed angle ($^\circ$) θ_r	Pointing shift (Δr) (μm)	Number of quads (northern + southern)	Defocus distance (cm)
1	23.5	23.5	0	8	1.0
2	30.0	35.0	96	8	1.0
3a	44.5	46.0	29	8	1.5
3b	44.5	69.0	456	8	1.0
4	50.0	86.0	647	16	1.0

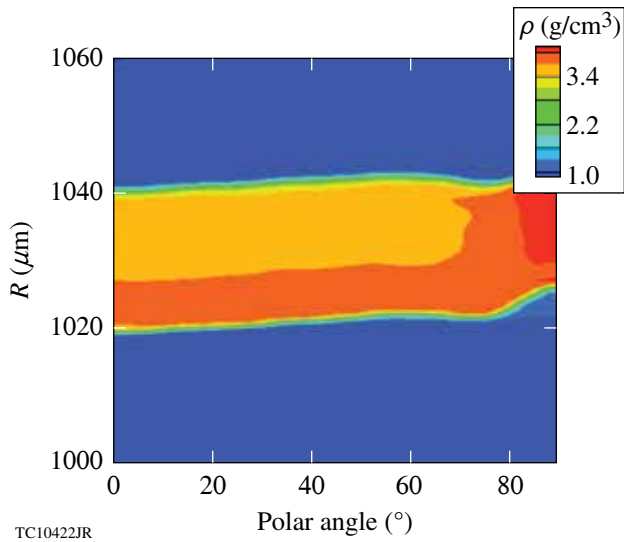


Figure 133.26
Mass-density contour at shock breakout (1.5 ns) versus radius and polar angle. The shock is largely uniform except near the equator.

Symmetry in the early stages of the implosion will be diagnosed using gated x-ray framing camera images of self-emission.³⁹ Photon energies $h\nu \geq 2$ keV from self-emission preferentially diagnose the imploding capsule outside the ablation surface.³⁹ For the three shell shapes, simulated images are shown in Fig. 133.27 at 7.2 ns—the latest time of observation corresponding to the end of the laser pulse. The *DRACO* simulations are post-processed with *Spect3D* including the pinhole diameter (100 μm), which is expected to be used in the initial experiments. Observable differences are predicted, as seen from Fig. 133.28, where the normalized amplitude of Legendre mode $\ell = 2$ is plotted versus time. The shaded regions include results from three simulations for each shape, where other long-wavelength nonuniformities⁴ such as beam mistiming (30-ps rms), beam mispointing (50- μm rms), and energy imbalance (8% rms) are included in the simulation. The deliberate asymmetries imposed in the PD designs dominate over the other nonuniformity seeds.

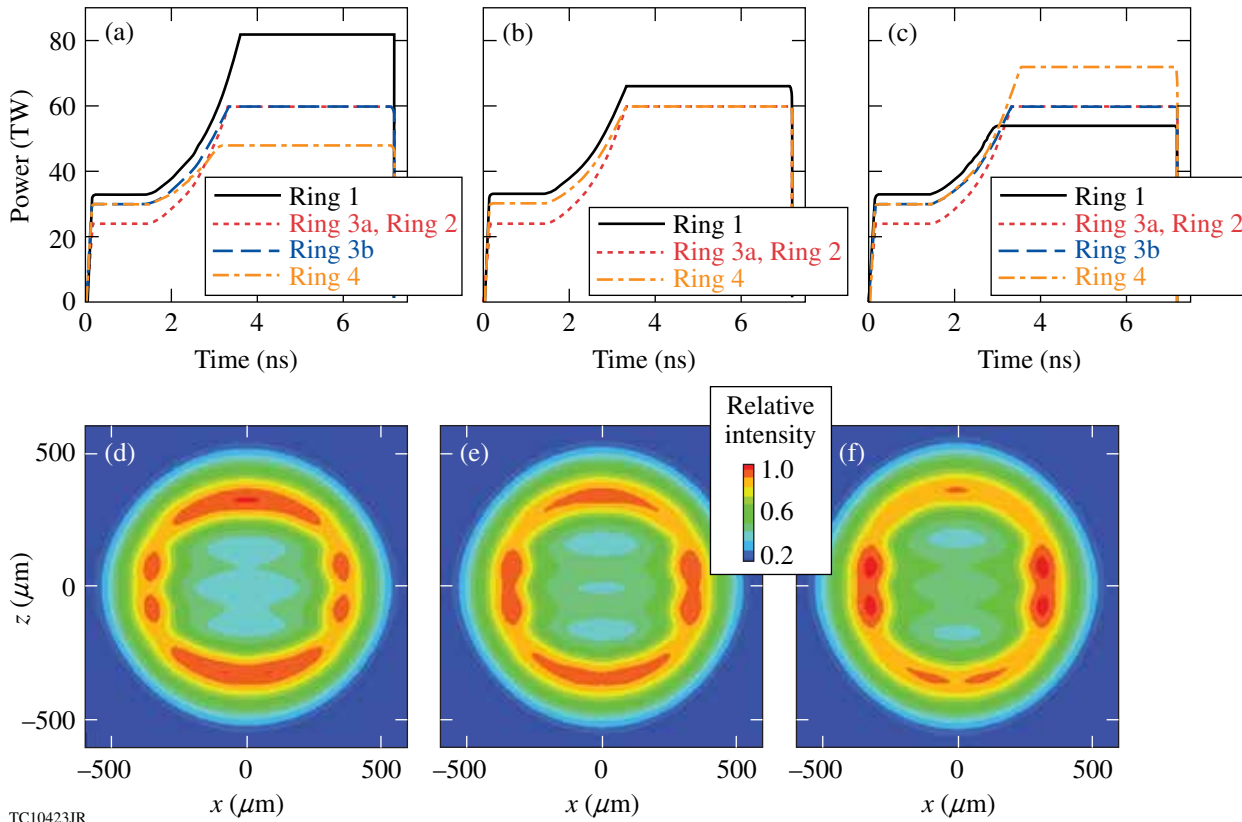


Figure 133.27
[(a)–(c)] Variations in pulse shapes used to achieve different shapes of the converging shell: (a) prolate, (b) spherical, and (c) oblate. The peak power of the pulse is varied with the shock strengths kept the same. [(d)–(f)] Corresponding x-ray gated framing-camera images from self-emission for $h\nu \geq 2$ keV.

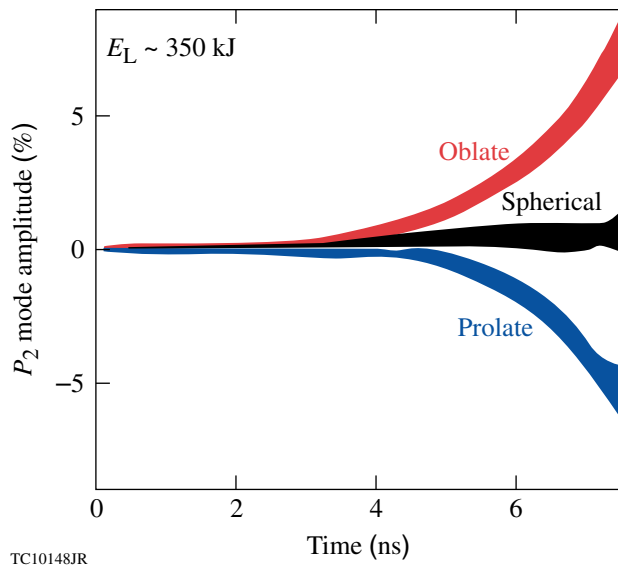


Figure 133.28

Relative amplitude (ratio of amplitude of Legendre mode $\ell = 2$ to shell position) versus time for the three shapes in Fig. 133.27. The shaded areas correspond to uncertainties associated with errors in beam timing, pointing, and energy balance.

Conclusions

The goal of OMEGA and NIF experiments is to validate physics models used to design PD ignition capsules and implement mitigating strategies for laser–plasma interactions. Laser-energy deposition and heat conduction are physics issues that need to be addressed at both OMEGA and NIF scales. In addition, it will be critical to understand issues related to preheat from energetic electrons produced by two-plasmon decay at the NIF scale. OMEGA PD experiments with emphasis on adiabat and symmetry were presented and observations compared with *DRACO* simulations. Two different pulse shapes were studied and it was found that areal density and symmetry are modeled well. Near-term PD experiments on OMEGA will be used to study PD target performance at ignition-relevant intensities. Initial NIF experiments are also discussed. The goal of these early experiments is to understand and address issues relating to the effect of two-plasmon decay on preheat and cross-beam energy transfer on implosion energetics and potentially symmetry.

ACKNOWLEDGMENT

This work was supported by the U.S. Department of Energy Office of Inertial Confinement Fusion under Cooperative Agreement No. DE-FC52-08NA28302, the University of Rochester, and the New York State Energy Research and Development Authority. The support of DOE does not constitute an endorsement by DOE of the views expressed in this article.

REFERENCES

1. S. Skupsky, J. A. Marozas, R. S. Craxton, R. Betti, T. J. B. Collins, J. A. Delettrez, V. N. Goncharov, P. W. McKenty, P. B. Radha, T. R. Boehly, J. P. Knauer, F. J. Marshall, D. R. Harding, J. D. Kilkenny, D. D. Meyerhofer, T. C. Sangster, and R. L. McCrory, *Phys. Plasmas* **11**, 2763 (2004).
2. E. Moses, presented at The Seventh International Conference on Inertial Fusion Sciences and Applications, Bourdeaux-Lac, France, 12–16 September 2011.
3. T. J. B. Collins, J. A. Marozas, K. S. Anderson, R. Betti, R. S. Craxton, J. A. Delettrez, V. N. Goncharov, D. R. Harding, F. J. Marshall, R. L. McCrory, D. D. Meyerhofer, P. W. McKenty, P. B. Radha, A. Shvydky, S. Skupsky, and J. D. Zuegel, *Phys. Plasmas* **19**, 056308 (2012).
4. T. J. B. Collins, J. A. Marozas, and P. W. McKenty, *Bull. Am. Phys. Soc.* **57**, 155 (2012).
5. M. C. Herrmann, M. Tabak, and J. D. Lindl, *Nucl. Fusion* **41**, 99 (2001).
6. Lord Rayleigh, *Proc. London Math Soc.* **XIV**, 170 (1883); G. Taylor, *Proc. R. Soc. London Ser. A* **201**, 192 (1950).
7. C. D. Zhou and R. Betti, *Phys. Plasmas* **14**, 072703 (2007).
8. P. B. Radha, C. Stoeckl, V. N. Goncharov, J. A. Delettrez, D. H. Edgell, J. A. Frenje, I. V. Igumenshchev, J. P. Knauer, J. A. Marozas, R. L. McCrory, D. D. Meyerhofer, R. D. Petrasso, S. P. Regan, T. C. Sangster, W. Seka, and S. Skupsky, *Phys. Plasmas* **18**, 012705 (2011).
9. T. C. Sangster, V. N. Goncharov, R. Betti, T. R. Boehly, R. Epstein, C. Forrest, V. Yu. Glebov, S. X. Hu, I. V. Igumenshchev, D. H. Froula, R. L. McCrory, D. D. Meyerhofer, P. B. Radha, W. Seka, W. T. Shmayda, S. Skupsky, C. Stoeckl, J. A. Frenje, D. T. Casey, and M. Gatu-Johnson, *Bull. Am. Phys. Soc.* **57**, 200 (2012).
10. *LLE Review Quarterly Report* **130**, 72, Laboratory for Laser Energetics, University of Rochester, Rochester, NY, LLE Document No. DOE/NA/28302-1058 (2012).
11. P. B. Radha, J. A. Marozas, F. J. Marshall, A. Shvydky, T. J. B. Collins, V. N. Goncharov, R. L. McCrory, P. W. McKenty, D. D. Meyerhofer, T. C. Sangster, and S. Skupsky, *Phys. Plasmas* **19**, 082704 (2012).
12. F. J. Marshall, P. W. McKenty, J. A. Delettrez, R. Epstein, J. P. Knauer, V. A. Smalyuk, J. A. Frenje, C. K. Li, R. D. Petrasso, F. H. Séguin, and R. C. Mancini, *Phys. Rev. Lett.* **102**, 185004 (2009).
13. P. B. Radha, F. J. Marshall, T. R. Boehly, T. J. B. Collins, R. S. Craxton, R. Epstein, V. N. Goncharov, J. A. Marozas, R. L. McCrory, P. W. McKenty, D. D. Meyerhofer, T. C. Sangster, A. Shvydky, S. Skupsky, J. A. Frenje, and R. D. Petrasso, “Polar Drive on OMEGA,” submitted to the *European Physical Journal*.
14. V. N. Goncharov, T. C. Sangster, T. R. Boehly, S. X. Hu, I. V. Igumenshchev, F. J. Marshall, R. L. McCrory, D. D. Meyerhofer, P. B. Radha, W. Seka, S. Skupsky, C. Stoeckl, D. T. Casey, J. A. Frenje, and R. D. Petrasso, *Phys. Rev. Lett.* **104**, 165001 (2010); P. B. Radha, J. A. Marozas, F. J. Marshall, A. Shvydky, T. J. B. Collins, V. N. Goncharov, R. L. McCrory, P. W. McKenty, D. D. Meyerhofer, T. C. Sangster, and S. Skupsky, *Phys. Plasmas* **19**, 082704 (2012).

15. S. Skupsky, R. W. Short, T. Kessler, R. S. Craxton, S. Letzring, and J. M. Soures, *J. Appl. Phys.* **66**, 3456 (1989).
16. T. R. Boehly, V. A. Smalyuk, D. D. Meyerhofer, J. P. Knauer, D. K. Bradley, R. S. Craxton, M. J. Guardalben, S. Skupsky, and T. J. Kessler, *J. Appl. Phys.* **85**, 3444 (1999).
17. F. H. Séguin, C. K. Li, J. A. Frenje, D. G. Hicks, K. M. Green, S. Kurebayashi, R. D. Petrasso, J. M. Soures, D. D. Meyerhofer, V. Yu. Glebov, P. B. Radha, C. Stoeckl, S. Roberts, C. Sorce, T. C. Sangster, M. D. Cable, K. Fletcher, and S. Padalino, *Phys. Plasmas* **9**, 2725 (2002).
18. P. B. Radha, V. N. Goncharov, T. J. B. Collins, J. A. Delettrez, Y. Elbaz, V. Yu. Glebov, R. L. Keck, D. E. Keller, J. P. Knauer, J. A. Marozas, F. J. Marshall, P. W. McKenty, D. D. Meyerhofer, S. P. Regan, T. C. Sangster, D. Shvarts, S. Skupsky, Y. Srebro, R. P. J. Town, and C. Stoeckl, *Phys. Plasmas* **12**, 032702 (2005).
19. J. A. Marozas, F. J. Marshall, R. S. Craxton, I. V. Igumenshchev, S. Skupsky, M. J. Bonino, T. J. B. Collins, R. Epstein, V. Yu. Glebov, D. Jacobs-Perkins, J. P. Knauer, R. L. McCrory, P. W. McKenty, D. D. Meyerhofer, S. G. Noyes, P. B. Radha, T. C. Sangster, W. Seka, and V. A. Smalyuk, *Phys. Plasmas* **13**, 056311 (2006).
20. R. C. Malone, R. L. McCrory, and R. L. Morse, *Phys. Rev. Lett.* **34**, 721 (1975).
21. J. Delettrez, *Can. J. Phys.* **64**, 932 (1986).
22. R. A. Lerche, D. W. Phillion, and G. L. Tietbohl, *Rev. Sci. Instrum.* **66**, 933 (1995).
23. P. B. Radha, J. A. Delettrez, R. Epstein, S. Skupsky, J. M. Soures, S. Cremer, and R. D. Petrasso, *Bull. Am. Phys. Soc.* **44**, 194 (1999).
24. R. Betti and C. Zhou, *Phys. Plasmas* **12**, 110702 (2005).
25. J. J. MacFarlane *et al.*, *High Energy Density Phys.* **3**, 181 (2007).
26. R. A. Forties and F. J. Marshall, *Rev. Sci. Instrum.* **76**, 073505 (2005).
27. J. D. Lindl, *Inertial Confinement Fusion: The Quest for Ignition and Energy Gain Using Indirect Drive* (Springer-Verlag, New York, 1998), p. 154.
28. I. V. Igumenshchev, D. H. Edgell, V. N. Goncharov, J. A. Delettrez, A. V. Maximov, J. F. Myatt, W. Seka, A. Shvydky, S. Skupsky, and C. Stoeckl, *Phys. Plasmas* **17**, 122708 (2010).
29. J. A. Marozas and T. J. B. Collins, *Bull. Am. Phys. Soc.* **57**, 344 (2012).
30. A. Simon, R. W. Short, E. A. Williams, and T. Dewandre, *Phys. Fluids* **26**, 3107 (1983).
31. C. Stoeckl, R. E. Bahr, B. Yaakobi, W. Seka, S. P. Regan, R. S. Craxton, J. A. Delettrez, R. W. Short, J. Myatt, A. V. Maximov, and H. Baldis, *Phys. Rev. Lett.* **90**, 235002 (2003).
32. P. B. Radha, J. P. Knauer, T. C. Sangster, V. N. Goncharov, I. V. Igumenshchev, R. Betti, R. Epstein, D. D. Meyerhofer, and S. Skupsky, *Bull. Am. Phys. Soc.* **52**, 143 (2007).
33. C. Stoeckl, P. B. Radha, R. E. Bahr, J. A. Delettrez, D. H. Edgell, V. Yu. Glebov, V. N. Goncharov, I. V. Igumenshchev, T. C. Sangster, W. Seka, J. A. Frenje, and R. D. Petrasso, *Bull. Am. Phys. Soc.* **56**, 241 (2011).
34. M. N. Rosenbluth, *Phys. Rev. Lett.* **29**, 565 (1972).
35. D. A. Russell and D. F. DuBois, *Phys. Rev. Lett.* **86**, 428 (2001).
36. L. Divol, LLNL, private communication (2012).
37. A. M. Cok, R. S. Craxton, and P. W. McKenty, *Phys. Plasmas* **15**, 082705 (2008).
38. J. A. Marozas, S. P. Regan, J. H. Kelly, D. D. Meyerhofer, W. Seka, and S. Skupsky, *J. Opt. Soc. Am. B* **19**, 7 (2002).
39. D. T. Michel, C. Sorce, R. Epstein, N. Whiting, I. V. Igumenshchev, R. Jungquist, and D. H. Froula, *Rev. Sci. Instrum.* **83**, 10E530 (2012).